Modeling bicarbonate formation in an alkaline solution with multi-level quantum mechanics/molecular dynamics simulations

Benjamin Bobell, Jan-Niklas Boyn, John Mark P. Martirez & Emily A. Carter

View supplementary material

Published online: 12 Jul 2024.

Submit your article to this journal

View related articles

View Crossmark data

Taylor & Francis
Taylor & Francis Group

Check for updates

CICCOTTI SPECIAL ISSUE (BY INVITATION ONLY)

Modeling bicarbonate formation in an alkaline solution with multi-level quantum mechanics/molecular dynamics simulations

Benjamin Bobell [a], Jan-Niklas Boyn[b], John Mark P. Martirez [c] and Emily A. Carter [b,c,d]

aDepartment of Physics, Princeton University, Princeton, NJ, USA; bDepartment of Mechanical and Aerospace Engineering, Princeton University, Princeton, NJ, USA; cPrinceton Plasma Physics Laboratory, Applied Materials and Sustainability Sciences, Princeton, NJ, USA; dAndlinger Center for Energy and the Environment, Princeton University, Princeton, NJ, USA

ABSTRACT

Understanding carbonate speciation and how it may be modulated is essential for the advancement of carbon dioxide (CO_2) capture and storage technologies, which often rely on the transformation of CO_2 into carbonate, e.g. via the formation of carbonate minerals. To date, few atomic-level, quantum-mechanics-based simulations have been carried out to characterize how carbonic acid (H_2CO_3) and bicarbonate (HCO_3^-) form in aqueous solution, and how pH affects this process. Recently, Martirez and Carter utilized rare-event sampling density functional theory molecular dynamics simulations in combination with multi-level embedded correlated wavefunction theory, thus accounting for both solvent dynamics and electron correlation accurately, to elucidate the mechanism of H_2CO_3 formation in neutral solution (*J. Am. Chem. Soc.*, 145, 12561, 2023). Here, we perform a complementary simulation using the same method to map out the energetics of HCO_3^- formation from dissolved CO_2 in basic solution. We find that, as in H_2CO_3 formation, including water dynamics is important to obtain an accurate prediction of the energetics for the aforementioned reaction. Furthermore, only with MD did we identify the correct pathway for the reaction, in which water – not hydroxide – acts as the initial nucleophile and only at the transition state does it lose a proton.

$CO_2 + OH^- \rightarrow HCO_3^-$

Embed

Blue Moon Ensemble DFT-MD + Embedded MP2
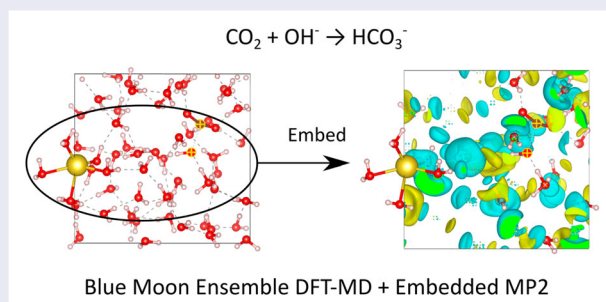
Introduction

Carbon capture, utilisation, and storage (CCUS) will be a crucial component in limiting global warming to under 2 °C by 2100 [1–3] – the goal set by the United Nations to limit the damage caused by anthropogenic climate change. [4] Without considering utilisation, two general flavours of CCS technologies are being pursued: in-situ and ex-situ methods. In-situ CCS involves injecting carbon dioxide (CO_2) underground, where it reacts with alkaline minerals in the local geological environment and forms solid carbonate compounds. In contrast, ex-situ techniques involve above ground mineralisation techniques that also safely store atmospheric CO_2 as a stable solid. [5] Common in-situ techniques include injecting CO_2 in basalt or clays [5,6], while common ex-situ techniques generally include converting CO_2 into carbonates through various industrial processes, which can either be stored or used in construction materials [5,7,8].

A particularly appealing form of CCUS accelerates the ocean's natural carbon sequestration process. Exploiting the fact that the oceans are one of the largest natural carbon sinks, containing approximately 40% of

anthropogenic carbon emissions [9], this process also mineralises CO_2 into carbonates [3,10–13]. The mineralisation process relies on speciation of aqueous CO_2 into carbonic acid (H_2CO_3), bicarbonate (HCO_3^-), and carbonate (CO_3^{2-}), with the latter reacting with Mg^{2+} and Ca^{2+} cations to form $Mg/Ca(CO_3)(s)$ phases. An alkaline environment can accelerate CO_2 mineralisation in a solution containing Ca^{2+} and Mg^{2+} ions by increasing the concentration of CO_3^{2-} relative to HCO_3^-, H_2CO_3, and dissolved CO_2 [3,14]. Due to its relative ease and efficiency, seawater electrolysis producing H_2 gas and locally high alkalinity at the cathode could become a fundamental component for large-scale ex-situ CO_2 mineralisation facilities [3,12,14]. Here, a technology derived from a single-step carbon sequestration and storage (sCS^2) concept, proposed by La Plante et al. [3,14], is especially promising [15]. In sCS^2, mesh electrodes facilitate precipitation of various carbonates, including calcium carbonate ($CaCO_3$) and magnesium carbonate ($MgCO_3$), yielding several advantages over alternative methods because it is: (i) significantly faster than in-situ methods (e.g. ref [6]), (ii) energy and cost-efficient, (iii) logistically simple, as it requires minimal infrastructure for CO_2 transportation, and (iv) is available for many different atmospheric CO_2 concentrations [3]. For sCS^2, the presence of in-situ sodium hydroxide (NaOH) in seawater aids carbonate precipitation by increasing the pH to form CO_3^{2-} and the saturation ratio of calcite [3,14]. Alternatively, wet scrubbing of CO_2 has been utilised for CCS demonstrations for more than a decade, in which CO_2 is absorbed into a solution of NaOH to form sodium carbonate (Na_2CO_3). [16–20]. The resulting sodium carbonate reacts with calcium hydroxide ($Ca(OH)_2$) to form $CaCO_3$, which is subsequently filtered [17,20].

A complete theoretical description of the dynamics of carbonate speciation in an alkaline solution, which are among the most fundamental steps leading up to carbonate mineralisation, could assist with designing and further improving future CCUS technologies. While experimental studies of the hydration of CO_2 in neutral and alkaline solutions have been carried out [21,22], computational simulations of carbonate speciation have focused largely on the hydration of aqueous CO_2 in neutral solution [23–30]. This includes both static simulations, in which Møller-Plesset second-order perturbation theory (MP2), coupled-cluster singles and doubles with perturbative triples (CCSD[T]), and density functional theory (DFT) have been utilised [28,29], and dynamic simulations utilising DFT molecular dynamics (MD) [26,30] and quantum mechanics-molecular mechanics (QM/MM) simulations [24,25]. However, recent research utilising multi-level embedded correlated wavefunction

(ECW) simulations demonstrated the need to capture simultaneously a correct description of charge separation at the transition state, as well as structural and solvent dynamics, in order to accurately reproduce the experimental free energetics of carbonic acid formation from CO_2 (at neutral pH) [23]. Although some steps have been made towards a theoretical understanding of carbonate speciation in an alkaline environment, those studies are significantly more limited. For example, Stirling observed reversible bicarbonate formation at high pH using DFT-MD, with the predicted activation free energy of HCO_3^- formation having significant positive entropic contributions while the activation free energy of decomposition back to CO_2 was predicted to be substantially endothermic [31]. Other relevant prior simulations include the use of DFT-MD and gas-phase MP2 to model nucleophilic attack of OH^- on CO_2 in water [32], and DFT-MD modelling of HCO_3^- formation in aqueous amine solvents [33–36]. These bodies of work, however, leave key mechanistic aspects of HCO_3^- formation in alkaline solution unexplored. These missing mechanistic details include the role of proton transfers during the reaction and, consequently, the identity of the nucleophile, as well as the interplay between structural dynamics and electron correlation effects that we have shown to be critical to describing CO_2 speciation in water [23].

In this article, we utilise a multi-level simulation scheme, combining DFT-MD with ECW methods and rare-event sampling, previously applied successfully to model CO_2 dissolution and reaction in neutral water, to simulate the formation of HCO_3^- from CO_2 dissolved in water containing hydroxide ion (OH^-). We demonstrate the ability of ECW simulations to correct fundamental errors in a DFT generalised gradient approximation exchange–correlation (DFT-GGA XC) functional, yielding good agreement with experimental reference data. We also shed new light on the mechanism of HCO_3^- formation in alkaline solution, with the somewhat surprising revelation that despite OH^- being the better nucleophile, the reaction proceeds via water rather than OH^- ion attack, followed by deprotonation at the transition state (TS).

Methodology

The overall modelling scheme we utilised in this work consists of three distinct steps: first, we generated eight structures connecting the reactants, TS, and product utilising a transition-state-search method and implicitly solvated static models. These structures serve as initial guess structures of the solute for the subsequent MD simulations. Second, for each structure derived from the first step we performed constrained, enhanced sampling

DFT-MD simulations utilising the blue-moon ensemble [37] in a large supercell containing the solutes and 53 water molecules, thereby explicitly and fully solvating the solute species along the reaction coordinate. Finally, to correct for errors in the electronic energy calculated at the DFT level, corrections to the internal energy component of the free energy are obtained using ECW theory for a select set of structures of the reactant, TS, and product within their respective constrained MD trajectories [23]. Further details of each of these steps are outlined below.

All periodic boundary condition DFT simulations were carried out using the Vienna Ab Initio Simulation Package (VASP) version 5.4.4 [38], utilising the all-electron, frozen core, projector augmented-wave (PAW) [39,40] method. We used standard PAW potentials for H, C, and O, where only the valence s and p orbitals are self-consistently solved for (only 1s for H). For Na, we used a version in which the semi-core 2p electrons are also self-consistently solved. We utilised for all calculations a 660-eV kinetic energy cutoff for the planewave basis while sampling only the Γ-point of the Brillouin zone with a Gaussian electronic smearing of width 0.01 eV. We performed constant particle-volume-temperature (NVT) MD using the Nosé-Hoover thermostat set to 300 K with a Nosé mass corresponding to a temperature oscillation frequency with a period of 40 MD steps [41,42].

To set up an initial reaction model for bicarbonate formation in alkaline solution, we first generated 11 static structures along the reaction pathway $CO_2 + OH^- \rightarrow HCO_3^-$ using a mixed explicit-implicit solvation model, in which we included a minimal set of explicit water molecules to solvate the ions along with continuum solvation, in order to capture both short- and long-range solvent effects. Some of these structures became the initial guess structures for the fully solvated solute along the reaction path in the ensuing constrained MD (*vide infra*). Specifically, we used a $20 \times 20 \times 20$ Å^3 periodic box containing CO_2, partly solvated hydroxide $[OH^- (H_2O)_2]$, and solvated sodium ion $[Na^+ (H_2O)_5]$, as the reactant composition; and solvated bicarbonate anion $[HCO_3^- (H_2O)_2]$ and the same $Na^+ (H_2O)_5$, as the product composition. We chose the box size to be large enough to have minimal interaction between each periodic image and to enable the counter cation (Na^+) and the anion (OH^- or HCO_3^-) to remain far apart, in order to evaluate the pure reaction energetics without spurious contribution from any randomly occurring ion-pairing interactions (Fig. S1).

We chose $[OH^- (H_2O)_2]$ as the nucleophile because OH^- would be the instinctive choice in alkaline solution. In the subsequent MD simulations, we investigated the effects of both constraining and not constraining the identity of the nucleophile (*vide infra*). Furthermore, although in liquid water OH^- is maximally solvated by three or four water molecules, each hydrogen-bonded to an O lone pair [43,44], OH^- has to shed one water molecule to free up a lone pair to attack the C atom of CO_2. We therefore chose two explicit water molecules as a first-shell solvation environment as the simplest model for the solvated OH^- in the reactant. By so doing, the resultant product, $[HCO_3^- (H_2O)_2]$, also then maintains a consistent number of hydrogen bonds with the explicit water molecules, with the C-OH moiety doubly hydrogen-bonded. The choice of two explicit solvating waters ensures that the number of explicit hydrogen bonds are consistent across the reaction and thus do not unnecessarily influence the energetics. We note that full solvation is accounted for in the subsequent MD simulations (*vide infra).*

We optimised reactant and product structures using spin-restricted DFT with the revPBE XC functional [45] and Grimme D3 van der Waals corrections with Becke–Johnson damping (D3BJ) [46,47], in a dielectric polarisable continuum model (DPCM) [48]. To compute the Helmholtz free energy barrier, we created a discrete set of six configurations connecting the reactant and product structures (a total of eight structures) by optimising a minimum energy pathway (MEP) using the climbing image nudged elastic band (CI-NEB) method [49]. The MEP was defined further with five linearly interpolated structures in between select CI-NEB images (Figures S1 and S2).

Next, to generate initial configurations for DFT-MD simulations, we used the solutes $CO_2 + OH^- (H_2O)_2$ for the reactant and $HCO_3^- (H_2O)_2$ for the product and the related intermediate structures along the MEP path (*vide supra*), to replace a hydroxide ion and three water molecules ($OH^- + 3H_2O$) in a periodic $12.2826 \times 11.8162 \times 11.545$ Å^3 simulation cell containing one hydroxide ion, one sodium ion, and 54 water molecules. This simulation cell was based on a pure water simulation of 56 H_2O molecules at their experimental room-temperature density, yielding 1 M concentrations of the solute (reactant, product, and intermediate structures). This simulation cell of $OH^- + Na^+ + 54 H_2O$ was pre-equilibrated for 25 ps using a 0.25 fs timestep within DFT-revPBE-D3BJ at a temperature of 300 K; more details of the MD are given below. This procedure yields CO_2 and OH^- or HCO_3^- with 53 H_2O molecules and Na^+ as the counter ion ($CO_2 + OH^- + Na^+ + 53H_2O$). Of the 13 refined MEP structures (Figure S1), we discarded three product-like structures due to redundancy for a total of nine unique structures. After initial insertion of the aforementioned fragments into the periodic cell of liquid water, we partially optimised the nine

initial structures using a quasi-Newton algorithm [50] until the maximum atomic forces were converged to 0.05 eV/Å. All atoms were allowed to relax except for the CO_2 and OH^- species; the O_2C - OH bond distance and the CO_2 angle were fixed to the value they adopted along the predicted MEP at each selected structure. The resulting constrained structures then were pre-equilibrated with NVT DFT-revPBE-D3BJ-MD for 35 ps at 0.5 fs timesteps at 300 K utilising the leap-frog Verlet algorithm [51]. Production simulations were carried out for an additional 35 ps using a 0.25-fs timestep, maintaining the O_2C - OH bond distance and CO_2 angle solute geometric constraints. To perform rare event sampling, we utilised the blue moon ensemble (BME) method [37,52], with collective variables (CV) associated with the constraints $\xi = (r_1, \theta)$ (the C-$O_{attacking}$ distance and the O-C–O angle of CO_2, respectively). The constraints were enforced with the SHAKE algorithm as implemented in VASP [53] and the change in the Helmholtz free energy between $\xi(a)$ and $\xi(b)$ ($\Delta F_{\xi(a) \to \xi(b)}$), where a and b are initial and final sets of coordinates, can be computed by numerical integration of the time-averaged free energy gradients ($\delta F / \delta \xi$) with respect to r_1 and θ. By sampling only a combination of r_1 and θ, we enable calculation of a one-dimensional (1D) slice (free energy curve or FEC) of the otherwise two-dimensional (2D) space (free energy surface) defined by r_1 and θ. This is valid because free energy is path independent. We therefore define the reaction coordinate (RC) as the cumulative length of line segments within the 2D space defined by r_1 and θ, connecting the reactant to the product and intermediate structures:

$$RC = \sum_{j=1}^{M-1} \sqrt{(r_{1,j+1} - r_{1,j})^2 + (\theta_{j+1} - \theta_j)^2} \quad (1)$$

where r_1 and θ are in Å and rad, respectively. M is the number of sampled structures (image number) from the reactant ($j = 1$) with a maximum value equal to the total number of sampled structures to reach the product. Because we are only seeing a 1D slice and the TS using static models is not necessarily the same as in the dynamic model (as turns out to be the case, Figure S2), we needed to confirm that we indeed found the TS in the 2D space within DFT-MD by ensuring that the overall time-averaged derivative of the newly found TS with respect to both r_1 and θ is nearly zero. The gradients are displayed in the SI (Table S1). Because the gradients remain large when using the CV derived from static optimisation of the product, we obtained a corrective term to the free energy from a 15-ps BME-MD simulation with the CV constrained to the time-averaged CV

of HCO_3^- we obtained from a 30-ps unconstrained equilibrium DFT-MD simulation at the same temperature, specifically, $r_1 = 1.389$ Å and $\theta = 2.215$ rad (126.9 °). Hereafter, we will refer to this structure as 'P'.

Following convergence of the BME-MD FEC, we carried out ECW calculations [54,55] using density functional embedding theory (DFET) [56,57] implemented in a modified version of VASP 5.3.3 [58,59]. Note that the DFET code is now available for the current VASP version 6. The embedded region consisted of the CO_2, the attacking OH^-, and the Na^+ counterion to ensure charge neutrality, in addition to their solvation shells, defined by six waters around Na^+, six waters around CO_2, and four waters around OH^-, yielding embedded regions of $Na(HCO_3)(H_2O)_{16}$ and $Na(CO_2)(OH^-)(H_2O)_{16}$ (*vide infra*). The remaining water molecules in the periodic supercell thus defined the environment surrounding the embedded region. By including six explicit water molecules around CO_2 and an additional four waters around the attacking OH^-/H_2O in the embedded cluster for ECW calculations, we allow for the explicit treatment of all direct hydrogen-bonding interactions between the reacting species and their first solvation shell in the EMB-MP2 calculations. Outer solvation-sphere effects are captured through the DFT-MD simulations and, by proxy, the embedding potential, in the ECW simulations.

We solve for the embedded-region – environment interaction potential or embedding potential (V_{emb}) through DFET via an extended optimised effective potential procedure [60]. We obtain corrections to the relative free energies according to:

$$F_{ECW}^{MD} = F_{revPBE+D3BJ}^{MD}$$
$$+ \sum_{j=1}^{k} \frac{(E_{ECW}^I[V_{emb}] - E_{revPBE+D3BJ}^I[V_{emb}])_j}{k}$$
$$= F_{revPBE+D3BJ}^{MD} + \bar{\delta}_{emb}$$

where $F_{revPBE+D3BJ}^{MD}$ is the Helmholtz free energy obtained from the BME-DFT-MD simulation of the entire periodic supercell, $E_{ECW}^I[V_{emb}]$ and $E_{revPBE+D3BJ}^I[V_{emb}]$, respectively, denote the energies of the embedded region obtained with the ECW theory of choice and embedded DFT-revPBE-D3BJ. To obtain a correction averaged over the different solvent configurations sampled during the BME-MD simulations ($\bar{\delta}_{emb,}$), we average over eight snapshots ($k = 8$) chosen equally spaced apart along the 35-ps constrained trajectory at each structure (*vide infra*). We carried out ECW calculations using MP2 [61] with the def2-TZVP [62] basis set and density fitting, as implemented in MOLPRO version 2021.2 [63]. Embedded MP2 was shown in our previous work studying dehydration dynamics of cations in water to reproduce higher

level embedded coupled-cluster theory free energies at lower cost [64] and therefore we employ it here.

Results

BME-MD simulations

We analysed the resulting BME FEC for the reaction $CO_2 + OH^- + Na^+ + 53H_2O \rightarrow HCO_3^- + Na^+ + 53 H_2O$ (*vide supra*) for convergence by integration over successive 5-ps increments of the trajectories using a 0.25 fs timestep, yielding FECs obtained after 5, 10, 15, 20, 25, 30, and 35 ps of simulation time for each of the nine non-redundant structures shown in Figure S1. These FECs are displayed in Figure 1 and reveal that fluxionality of the solvent molecules around the constrained $CO_2 + OH^-$ that evolves along the FEC has only a minor effect on free energetics of the reaction, with robust convergence of the FEC achieved after only 10 ps of averaging at each structure sampled along the MEP. We obtain a final forward free energy barrier height ($\Delta F^{\ddagger}_{forward}$) of 0.32 eV and reaction free energy (ΔF_{rxn}) of $-$ 0.18 eV (when including a 0.07 eV correction due to the difference in the product CVs we derived from static optimisation vs. unconstrained MD, i.e. structure P), predicted at the DFT-revPBE-D3BJ level of theory. These values significantly underestimate the magnitudes of the experimentally determined Gibbs free energy barrier ($\Delta G^{\ddagger}_{forward}$) of 0.50 eV and reaction Gibbs free energy (ΔG_{rxn}) of $-$ 0.43 eV [21]. Note that here we compare our predicted ΔFs with experimental ΔGs because we expect that the change in the pressure-volume energy term to be negligible for reactions in dilute solutions. Although quantitatively inaccurate, the predictions are in line with the experimentally observed reduction in the free energetics when moving to alkaline conditions, i.e. when OH^- is the nucleophile in lieu of H_2O ($\Delta G^{\ddagger}_{forward} = 0.95$ eV and $\Delta G_{rxn} = 0.28$ eV for H_2O as nucleophile) [21]. Specifically, Martirez and Carter calculated using a similar model and the same DFT-BME-MD method that the $CO_2 + H_2O \rightarrow H_2CO_3$ reaction has $\Delta F^{\ddagger}_{forward}$ and ΔF_{rxn} of 0.66 and 0.14 eV, respectively [23].

To investigate possible effects on the energetics of CO_2 speciation arising from the presence of Na^+, the proximity of the counterion to CO_2/ HCO_3^- was analysed across the surveyed trajectories along the reaction path. We monitored the C-Na distance (R(C-Na)) during DFT-MD for each constrained structure along the reaction path (indices in Figure 1 denote individual structures and their CVs are displayed in Figure S1) and averaged its values over 5-ps simulation intervals (Figure S3). Time-averaged R(C-Na)s reveal a tendency toward formation of a solvent-shared and in some instances a contact ion
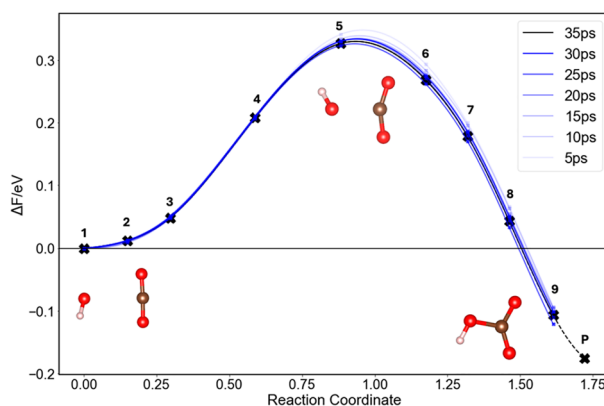

Figure 1. FEC and its convergence as a function of total simulation time at each point sampled along the $CO_2 + OH^- \rightarrow HCO_3^-$ reaction, obtained from BME-MD simulations at the DFT-revPBE-D3BJ level of theory. The dashed black line (with structure P) represents the final FEC. The reaction coordinate was evaluated using Eq. 1. Inset: reactant, TS, and product (image 9) structures showing only the reacting species. C: brown, O: red, and H: white spheres. Numbers indicate the individual constrained structures sampled along the reaction path.

pair (SSHIP and CIP, respectively) between Na^+ and HCO_3^- at and after the TS, although we detected no long-lived Na^+-HCO_3^- contact-ion pair in our simulations of the product. Unsurprisingly, CO_2 and Na^+ do not have such a tendency for close contact leading up to the TS. Further inspection of the R(C-Na) after the TS reveals significant fluxionality in the relative positions of the ions, with the frequent formation and dissociation of CIPs and SSHIPs. This strongly suggests relatively free movement of the Na^+ ion throughout the supercell with a low barrier to ion-pair formation and dissociation. This behaviour indicates that Na^+ does not play a significant role in HCO_3^- formation. To quantify the strength of the ion pairing and ascertain its effect on the energetics of HCO_3^- formation from CO_2, we performed additional constrained BME-MD simulations from the TS, i.e. with a fixed $\xi = (r_1, \theta)$ corresponding to the TS, and re-integrated the FEC at the TS as a function of R(C-Na). We sampled six fixed R(C-Na) values, namely, 2.93, 3.43, 4.23, 4.93, 5.93, and 6.93 Å, and performed 5-ps constrained MD (constraining also the original CVs as before) with 0.25-fs timesteps. The resulting FEC (function of R(C-Na), Figure S4) reveals two apparent minima at R(C-Na) = 4.23 Å and 5.93 Å at the TS, separated by a barrier of just 0.01 eV, confirming that Na^+-HCO_3^- ion pairing is an essentially barrierless and nearly thermoneutral process, with negligible influence on the speciation free energetics. To further quantify any possible effects on $\Delta F^{\ddagger}_{forward}$ as a result of the proximity of Na^+, we re-evaluated the BME-MD FEC as a function of $\xi = (r_1, \theta)$ from the reactant to TS for the different constant

R(C-Na) values listed above (Figure S5). The variation in $\Delta F^{\ddagger}_{forward}$ is at most 0.05 eV for different R(C-Na)s and the effect of the proximity of Na^+ is, thus, predicted to be negligible.

Next, we considered the effects of OH^- diffusion throughout the reaction pathway to form HCO_3^-. With only $\xi = (r_1, \theta)$ constrained, the attacking O is free to accept and donate protons as it pleases, becoming either H_2O or OH^- via proton transfer. Figure 2(a) displays the average distance of OH^- from the CO_2 carbon (R(C-OH^-)) as a function of R(C-$O_{attacking}$) averaged over each of the 35-ps trajectories (at each of the nine constrained structures sampled along the path). As expected, while the attacking oxygen was initialised as a OH^-, proton transfer occurs between water molecules prior to C–O bond formation in the TS. In structures 1, 3, 4, and 5 along the FEC in Figure 1 (see Figure S1 for structures), the attacking oxygen is always part of a water molecule, with the OH^- being preferentially located in the second hydration shell of the Na^+ counterion. In structure 2, the attacking oxygen moiety is a OH^- ion for the first half of the 35 ps trajectory, before converting to a water molecule in the second half of the trajectory, explaining the lower average observed R(C-OH^-). This likely is a statistical outlier with respect to the other surveyed structures along the reaction pathway and is a result of the limited timescales accessible to AIMD simulations. At the TS, with R(C-$O_{attacking}$) = 2.1 Å, significant bond formation has occurred between the incoming oxygen and the CO_2 molecule and a clear preference for attack by hydroxide is exhibited, with the attacking oxygen moiety being a water for only 6% of the 35 ps trajectory. Thus, a more complete picture of the reaction emerges. While the attacking species starts out nominally as OH^-, proton transfer enables it to alternate between being water and being hydroxide, and only once reaching the transition state does it more irreversibly acquire and keep its negative charge on the way to forming bicarbonate.

To delve further, we attempted to deconvolute the driving forces associated with this proton-mediated interconversion along the path to bicarbonate by evaluating the intrinsic solvation stabilisation of hydroxide driving water to be the initial reactant and by evaluating the intrinsic barrier for hydroxide attack with no proton exchange. To quantify the energetic penalty of restricting the OH^- to provide the attacking O throughout the surveyed structures along the reaction path, additional BME-MD trajectories were simulated, which imposed an additional constraint on the O-H coordination number of the attacking O. Structures 1 through 5 along the FEC (Figure 1, structures shown in Figure S1) were simulated for an additional 15 ps utilising this new constraint. Figure 2(b) compares the FEC obtained by integrating over the OH-constrained 15-ps trajectories in 5-ps increments with the FEC obtained from the above-mentioned simulations that did not place any constraints on the identity of the attacking oxygen moiety. Again, we observe good convergence after 10 ps of simulation time for each sampled constrained structure. Inspection of the FEC reveals significant destabilisation of the $OH^- + CO_2$ configurations at and near the reactant state with respect to the $H_2O + CO_2$ configuration. This energetic penalty is likely the result of both the loss of hydrogen bonding in constraining the OH^- to the first coordination shell around the CO_2, and its greater distance from the positively charged Na^+ counterion. The resulting 0.24 eV destabilisation of the reactants reduces the TS barrier to 0.08 eV for the case of CO_2 being attacked by OH^-, in lieu of H_2O. Not surprisingly, this almost barrierless prediction is consistent with the static model because OH^- in that simpler model was unable to accept a proton with only two explicit water molecules in its vicinity (Figure S2). These results also show that the intrinsic reaction of OH^- with CO_2 in solution is quite facile with a low barrier. It is the desolvation of OH^- and/or the intrinsic barrier for water reacting with CO_2 that leads to the free energy barrier being doubled.

ECW theory simulations

DFT-GGA XC functionals are known to be inaccurate for systems containing charge-separated species, because of their tendency to spuriously spread out (delocalise) electron density due to their intrinsic electron self-interaction error [65]. Consequently, we carried out ECW theory calculations with MP2 (EMB-MP2) for the critical points of the FEC (configurations 1, 5 and 9, i.e. the reactant, TS and product, respectively, structures shown in Figure 3). Because the DFET calculations to compute embedding potentials require charge neutrality in each subsystem (the potential optimisation is performed within periodic DFT), and to account accurately for both solvation effects and the interaction between the reacting moieties, the embedded region was defined as the CO_2 and its first solvation shell of six waters, and the OH^- and its first solvation shell of four waters, in addition to the Na^+ counterion and its first solvation shell of six waters. To reduce fluxionality of the embedded region and to ensure a consistent embedding approach, only the pathway constraining the attacking oxygen moiety to be a OH^- was considered (*vide supra*, Figure 2(b)). To obtain the overall free energy barrier, we then add the difference between the constrained and unconstrained OH^- reactant energies obtained within DFT-MD, assuming that the difference in free energies starting from OH^- versus H_2O attack are well captured at
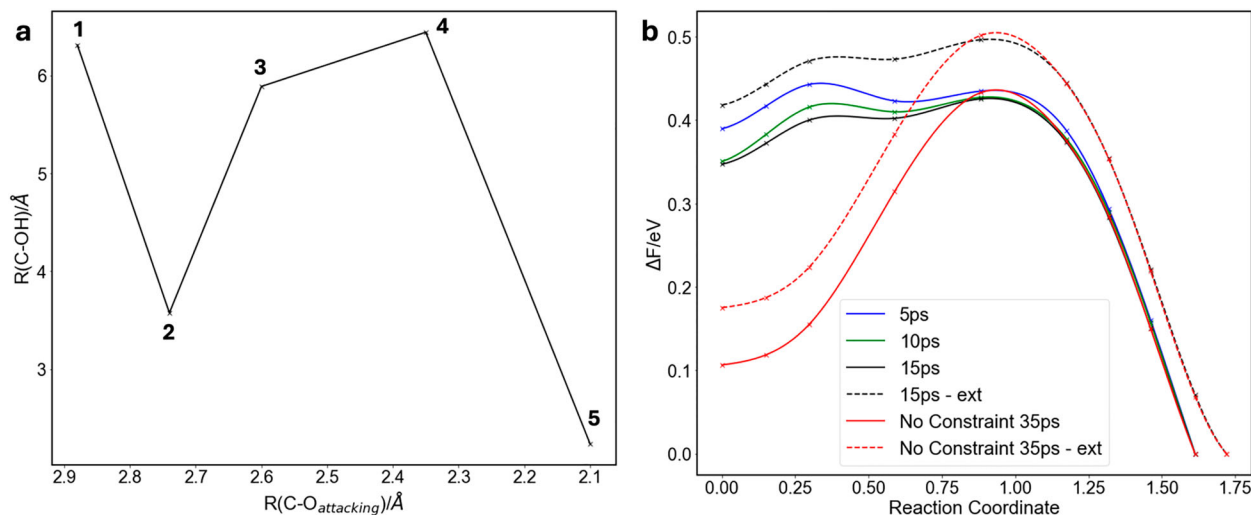
Figure 2. (**a**): Average distance between the carbonate carbon atom and the OH^- oxygen atom (R(C-OH)), as a function of the distance between the carbon dioxide carbon atom and the attacking oxygen atom, either in OH^- or H_2O (R(C-$O_{attacking}$)), both in Å. (**b**): FEC for the $CO_2 + OH^- \rightarrow HCO_3^-$ reaction, imposing a constraint upon the attacking oxygen, requiring it to be OH^- across all surveyed structures. Convergence is displayed as a function of simulation time for each constrained structure and the FECs are compared to the converged FEC obtained without constraints that the attacking nucleophile to be OH^-. Dashed lines (appended with ' – ext' in the label) show the FECs corrected for the final product CV (P) from the time-averaged CV from unconstrained DFT-MD. All data obtained from BME-MD simulations at the DFT-revPBE-D3BJ level of theory.

the DFT-revPBE-D3BJ level of theory, counting on some cancellation of error between those states to preserve accuracy. For each critical point, eight equally spaced configurations were chosen from the constrained BME-MD trajectory and the resulting EMB-MP2 single-point electronic energies were averaged to provide a correction to the DFT-revPBE-D3BJ BME-MD free energy. This methodology was utilised successfully in previous work to evaluate the free energetics of several related aqueous chemical processes, including the formation of H_2CO_3 from dissolved CO_2 [23], the dehydration of aqueous Mg and Ca cations [64] and the formation of Mg and Ca ion pairs with carbonate [66]. Note that only internal energies are corrected utilising this methodology. Because of the prohibitive cost of EMB-MP2 calculations, we can only use them for static calculations. We therefore must assume that DFT-MD provides correct structures and dynamics, capturing the non-internal energy components of the free energy correctly.

Figure 3 displays the EMB-MP2-corrected reaction coordinate diagram along with representative structures for the embedded region models of the reactants, TS, and product. Comparison to the DFT-revPBE-D3BJ-MD profile reveals a significant energy correction at the TS, with EMB-MP2 predicting a free energy barrier of $\Delta F_{EMB-MP2}^{TS} = 0.51$ eV (accounting for the reactant stabilisation of 0.24 eV, i.e. subtracting 0.24 eV from the reactant free energy, by removing the constraint imposed

on the attacking oxygen moiety to be OH^-), which is a 0.19 eV increase over the DFT-revPBE-D3BJ-MD result. In the case of the reaction free energy, the EMB-MP2 prediction of $\Delta F_{EMB-MP2}^{rxn} = -0.21$ eV (including a correction of – 0.07 eV from structure P) differs by only – 0.03 eV from the DFT-revPBE-D3BJ-MD result. The EMB-MP2 barrier is thus in almost exact agreement with experiment, while the reaction free energy remains an underestimation compared to the experimental reference values (Table 1).

To put our work in perspective, we compare in Table 1 free energies for the $OH^- + CO_2 \rightarrow HCO_3^-$ reaction obtained with the levels of theory utilised in this work and those previously reported in the literature for both HCO_3^- and H_2CO_3 formation from CO_2. The most directly analogous work to ours was conducted by Leung et al. [32] They simulated nucleophilic attack of CO_2 by OH^- utilising DFT-revPBE-MD with umbrella sampling and included several corrections to the free energies, aiming to account for errors in the zero-point energy, rotational entropy, and the electronic energy. These corrections were obtained from gas-phase MP2 calculations. Deviations between their pure DFT-MD results and ours are observed, with their results agreeing with ours to within 0.01 eV for $\Delta F_{forward}^{\ddagger}$ but differing by – 0.36 eV for ΔF_{rxn} (Table 1). This is likely the result of several key factors, including their lack of consideration of proton transfers (*vide supra*), the use of a uniform background
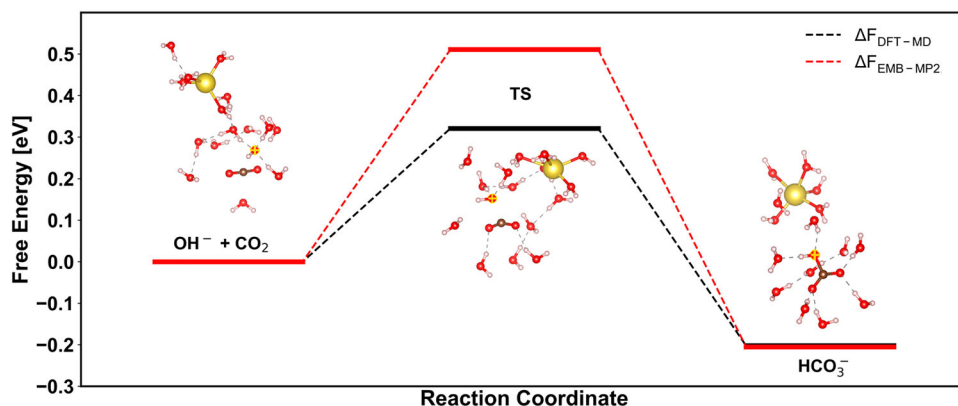
Figure 3. Reaction profile for the $CO_2 + OH^- \rightarrow HCO_3^-$ reaction, displaying the free energies of the TS and HCO_3^- product, relative to the $OH^- + CO_2$ reactants. Black lines show the BME-MD DFT-revPBE-D3BJ results, while red lines denote the EMB-MP2 corrected free energies. The reacting oxygen atom is highlighted with a yellow cross. Here the results are obtained by constraining the reactant to be OH^- at all times along the reaction path. We further correct the reactant and product energies by including the –0.24 eV reactant stabilization by allowing water to be the initial nucleophile and the product stabilization by –0.07 eV when using P as final product BME-DFT-MD energy. Insets: Na: yellow, C: brown, O: red, and H: white spheres.

Table 1. Free energetics (eV) obtained in this work and studies reported in the literature for both the $CO_2 + OH^- \rightarrow HCO_3^-$ and $CO_2 + H_2O \rightarrow H_2CO_3$ reactions.

	Charge/ counter ion	$\Delta F^{\ddagger}_{forward}$	$\Delta F^{\ddagger}_{reverse}$	ΔF_{rxn}
$CO_2 + OH^- \rightarrow HCO_3^-$				
Experiment[a] [21]		0.52 ± 0.02	0.97 ± 0.03	-0.45 ± 0.02
Periodic DFT-MD (DFT-revPBE-D3BJ, this work)	neutral/ Na$^+$	0.32	0.50	−0.18
Corrected periodic DFT-MD (DFT-revPBE-D3BJ) with open-boundary EMB-MP2 (this work)	neutral/ Na$^+$	0.51 ± 0.20	0.72 ± 0.22	-0.21 ± 0.12
Periodic DFT-MD (DFT-BLYP)[31]	neutral/ unclear	0.60	0.90	−0.30
Periodic DFT-MD (Umbrella Sampling revPBE) [32]	neutral/ positive uniform background charge	0.31	0.85	−0.54
Corrected periodic DFT-MD (Umbrella Sampling revPBE) with gas-phase open-boundary MP2 [32]	MD: neutral/ positive uniform background charge Gas phase: negative/none	0.42	0.85	−0.43
$CO_2 + H_2O \rightarrow H_2CO_3$				
Experiment[a] [21]		0.95 ± 0.03	0.68 ± 0.01	0.27 ± 0.03
Periodic DFT-MD (DFT-revPBE-D3BJ) [23]	neutral/ none	0.71	0.53	0.17
Corrected periodic DFT-MD (DFT-revPBE-D3BJ) with open-boundary EMB-MP2 [23]	neutral/ none	0.96 ± 0.04	0.63 ± 0.05	0.33 ± 0.04
Periodic DFT-MD (DFT-BLYP) [30]	neutral/ none	0.82	0.68	0.14

[a] From spectrophotometric stop-flow measurements. Eyring and van't Hoff fits (at T = 6.6–42.8 °C) were used to derive the free energies of activation and reaction, respectively.

charge instead of an explicit counterion, and the absence of dispersion corrections in their simulations, in addition to differences in sampling. Furthermore, their internal energy correction from gas-phase MP2 calculations using $[CO_2\text{-}OH^-]$, i.e. not including other contributions, differs in both sign and magnitude from our ECW-MP2 corrections, with corrections to the forward barrier of –0.11 eV, as compared to our +0.19 eV, and –0.33 eV as compared to our –0.03 eV for the reaction free energy. Here, simple gas-phase calculations on the $[CO_2\text{-}OH^-]$ system fail to account accurately for changes in the solvation environment of the reactive species, which in our EMB-MP2 calculations are captured through inclusion of 16 explicit water molecules in addition to the sampled embedding potentials. The only other previous

DFT-MD study on the $OH^- + CO_2 \rightarrow HCO_3^-$ reaction utilised the BLYP XC functional in combination with metadynamics sampling [31]. They uncharacteristically (for DFT-GGA) overestimated the TS barrier, while the reaction free energy lies –0.12 eV below that of our BME-DFT-MD revPBE-D3BJ-based simulations. This fortuitous agreement of the latter is likely the result of favourable error cancellation, arising from the use of low planewave basis kinetic energy cutoffs, a lack of dispersion corrections, limited sampling, and differences in how charge neutrality was achieved. Finally, comparing the free energetics of the HCO_3^- pathway in alkaline solution to the H_2CO_3 pathway in a neutral environment, we correctly predict a large reduction in the barrier to CO_2 speciation in an alkaline environment, as well as

the switch from an endo – to an exo-thermic process. The only other previous DFT-BLYP-MD study [30] of carbonic acid formation somewhat underestimated both the forward barrier and endoergicity, yielding an accurate backward barrier, while our multilevel simulation approach yielded free energy changes and barriers all within 0.05 eV of experiment [23].

Conclusions

We conducted multi-level, DFT-MD-based, ECW calculations to characterise the mechanism of CO_2 speciation to bicarbonate, in alkaline solution. Using BME-MD rare-event sampling, we demonstrated that the reaction preferentially occurs through initial attack by water rather than hydroxide, followed by deprotonation at the TS to form HCO_3^-. In contrast, H_2CO_3 formation involves a zwitterionic $H_2O – CO_2$ TS [23], which thus exhibits a higher reaction barrier. Importantly, we also demonstrate the ability of MD-sampled ECW calculations to eliminate some shortcomings of DFT GGA XC functionals commonly utilised for AIMD simulations of charged species in solution. Utilising EMB-MP2 calculations to correct the internal energy errors in the DFT-revPBE-D3BJ simulations, we significantly improve agreement with experiment, reproducing the experimentally determined forward free energy barrier. Residual errors on the order of ~ 5 kcal/mol remain for the free energy of reaction; these are likely due to limitations imposed upon AIMD simulations with respect to affordable supercell size that, correspondingly, limits the pH range, reactant and counterion concentrations, and time scales achievable. The data obtained in this study yield important insights into the mechanism of carbon dioxide speciation in alkaline environments, such as seawater, and provides valuable, ab-initio reference data for the energetics of these processes [23,64,66]. Finally, such data will play an important role in the development of machine-learned force fields for the simulation of longer length – and time-scale processes involved in carbonate mineralisation.

Acknowledgment

Disclosure statement

Funding

Author contributions

The manuscript was written through contributions of all authors. All authors have given approval to the final version of the manuscript.

ORCID

Benjamin Bobell http://orcid.org/0000-0003-4004-5070
John Mark P. Martirez http://orcid.org/0000-0003-0566-6605
Emily A. Carter http://orcid.org/0000-0001-7330-7554

References

[1] N. Mac Dowell, P.S. Fennell, N. Shah, and G.C. Maitland. Nat. Clim. Change. **7** (4), 243–249 (2017). doi: 10.1038/nclimate3231.

[2] J. Rissman, C. Bataille, E. Masanet, N. Aden, W.R. Morrow, N. Zhou, N. Elliott, R. Dell, N. Heeren, B. Huckestein, et al. Appl. Energy. **266**, 114848 (2020). doi:10.1016/j.apenergy.2020.114848.

[3] E.C. La Plante, D.A. Simonetti, J. Wang, A. Al-Turki, X. Chen, D. Jassby, and G.N. Sant, ACS Sustain. Chem. Eng. **9** (3), 1073–1089 (2021).

[4] Programme, U. N. E. Emissions Gap Report 2022; Nairobi, 2019.

[5] V. Romanov, Y. Soong, C. Carney, G.E. Rush, B. Nielsen, and W. O'Connor, ChemBioEng Reviews. **2** (4), 231–256 (2015). doi: 10.1002/cben.201500002.

[6] J.M. Matter, M. Stute, SÓ Snæbjörnsdottir, E.H. Oelkers, S.R. Gislason, E.S. Aradottir, B. Sigfusson, I. Gunnarsson, H. Sigurdardottir, E. Gunnlaugsson, et al., Science. **352** (6291), 1312–1314 (2016). doi:10.1126/science.aad8132.

[7] R. Zevenhoven, S. Eloneva and S. Teir, Catal. Today. **115** (1), 73–79 (2006). doi: 10.1016/j.cattod.2006.02.020.

[8] National Academies of Sciences, E., and Medicine. *Carbon Dioxide Utilization Markets and Infrastructure: Status and Opportunities: A First Report* (The National Academies Press, 2023). doi:10.17226/26703.

[9] C.L. Sabine and T. Tanhua, Ann. Rev. Mar. Sci. **2** (1), 175–198 (2010). doi:10.1146/annurev-marine-120308-080947.

[10] C. Hepburn, E. Adlen, J. Beddington, E.A. Carter, S. Fuss, N. Mac Dowell, J.C. Minx, P. Smith, and C.K. Williams,

Nature. **575** (7781), 87–97 (2019). doi:10.1038/s41586-019-1681-6.

[11] K.S. Lackner, C.H. Wendt, D.P. Butt, E.L. Joyce, and D.H. Sharp, Energy. **20** (11), 1153–1170 (1995). doi:10.1016/0360-5442(95)00071-N.

[12] R. Sharifian, L. Boer, R.M. Wagterveld, and D.A. Vermaas, Chem. Eng. J. **438**, 135326 (2022). doi:10.1016/j.cej.2022.135326.

[13] P. Renforth and G. Henderson, Rev. Geophys. **55** (3), 636–674 (2017). doi:10.1002/2016RG000533.

[14] E.C. La Plante, X. Chen, S. Bustillos, A. Bouissonnie, T. Traynor, D. Jassby, L. Corsini, D.A. Simonetti, and G.N. Sant, ACS ES&T Eng. **3** (7), 955–968 (2023). doi:10.1021/acsestengg.3c00004.

[15] UCLA Institute for Carbon Management and Equatic to Build the World's Largest Ocean-Based Carbon Removal Plant in Singapore. UCLA Samueli Newsroom: Online, 2024.

[16] S. Kar, A. Goeppert, V. Galvan, R. Chowdhury, J. Olah, and G.K.S. Prakash, J. Am. Chem. Soc. **140** (49), 16873–16876 (2018). doi:10.1021/jacs.8b09325.

[17] K.S. Lackner, EPJ ST. **176** (1), 93–106 (2009). doi:10.1140/epjst/e2009-01150-3.

[18] M. Mahmoudkhani and D.W. Keith, Int. J. Greenhouse Gas Control. **3** (4), 376–384 (2009). doi:10.1016/j.ijggc.2009.02.003.

[19] M. Yoo, S.-J. Han, and J.-H. Wee, J. Environ. Manag. **114**, 512–519 (2013). doi:10.1016/j.jenvman.2012.10.061.

[20] F. Zeman, Environ. Sci. Technol. **41** (21), 7558–7563 (2007). doi:10.1021/es070874 m.

[21] X. Wang, W. Conway, R. Burns, N. McCann, and M. Maeder, J. Phys. Chem. A. **114** (4), 1734–1740 (2010). doi:10.1021/jp909019u.

[22] A.H. England, A.M. Duffin, C.P. Schwartz, J.S. Uejio, D. Prendergast, and R.J. Saykally, Chem. Phys. Lett. **514** (4), 187–195 (2011). doi:10.1016/j.cplett.2011.08.063.

[23] J.M.P. Martirez and E.A. Carter, J. Am. Chem. Soc. **145** (23), 12561–12575 (2023). doi:10.1021/jacs.3c01283.

[24] N. Prasetyo and T.S. Hofer, J. Chem. Theory Comput. **14** (12), 6472–6483 (2018). doi:10.1021/acs.jctc.8b00557.

[25] A.V. Nemukhin, I.A. Topol, B.L. Grigorenko, and S.K. Burt, J. Phys. Chem. B. **106** (7), 1734–1740 (2002). doi:10.1021/jp0141629.

[26] P.P. Kumar, A.G. Kalinichev, and R.J. Kirkpatrick, J. Phys. Chem. B. **113** (3), 794–802 (2009). doi:10.1021/jp809069 g.

[27] G.A. Gallet, F. Pietrucci, and W. Andreoni, J. Chem. Theory Comput. **8** (11), 4029–4039 (2012). doi:10.1021/ct300581n.

[28] B. Wang and Z. Cao, J. Comput. Chem. **34** (5), 372–378 (2013). doi:10.1002/jcc.23144.

[29] M.T. Nguyen, M.H. Matus, V.E. Jackson, V.T. Ngan, J.R. Rustad, and D.A. Dixon, J. Phys. Chem. A. **112** (41), 10386–10398 (2008). doi:10.1021/jp804715j.

[30] A. Stirling, and I. Pápai, J. Phys. Chem. B. **114** (50), 16854–16859 (2010). doi:10.1021/jp1099909.

[31] A. Stirling, J. Phys. Chem. B. **115** (49), 14683–14687 (2011). doi:10.1021/jp2084204.

[32] K. Leung, I.M.B. Nielsen, and I. Kurtz, J. Phys. Chem. B. **111** (17), 4453–4459 (2007). doi:10.1021/jp068475 l.

[33] H.M. Stowe and G.S. Hwang, Phys. Chem. Chem. Phys. **19** (47), 32116–32124 (2017). doi:10.1039/C7CP05580C.

[34] H. Nakai, Y. Nishimura, T. Kaiho, T. Kubota, and H. Sato, Chem. Phys. Lett. **647**, 127–131 (2016). doi:10.1016/j.cplett.2016.01.059.

[35] K.Z. Sumon, A. Henni, and A.L.L. East, J. Phys. Chem. Lett. **5** (7), 1151–1156 (2014). doi:10.1021/jz500237v.

[36] Y. Matsuzaki, H. Yamada, F.A. Chowdhury, T. Higashii, and M. Onoda, J. Phys. Chem. A. **117** (38), 9274–9281 (2013). doi:10.1021/jp406636a.

[37] E.A. Carter, G. Ciccotti, J.T. Hynes, and R. Kapral, Chem. Phys. Lett. **156** (5), 472–477 (1989). doi:10.1016/S0009-2614(89)87314-2.

[38] G. Kresse and J. Fürthmuller, Phys. Rev. B. **54** (16), 11169–11186 (1996). doi:10.1103/PhysRevB.54.11169.

[39] P.E. Blochl, Phys. Rev. B. **50** (24), 17953–17979 (1994). doi:10.1103/PhysRevB.50.17953.

[40] G. Kresse and D. Joubert, Phys. Rev. B. **59** (3), 1758–1775 (1999). doi:10.1103/PhysRevB.59.1758.

[41] S. Nosé, J. Chem. Phys. **81** (1), 511–519 (1984). doi:10.1063/1.447334.

[42] W.G. Hoover, Phys. Rev. A. **31** (3), 1695–1697 (1985). doi:10.1103/PhysRevA.31.1695.

[43] M.E. Tuckerman, A. Chandra, and D. Marx, Acc. Chem. Res. **39** (2), 151–158 (2006). doi:10.1021/ar040207n.

[44] A. Botti, F. Bruni, S. Imberti, M.A. Ricci, and A.K. Soper, J. Chem. Phys. **120** (21), 10154–10162 (2004). doi:10.1063/1.1705572

[45] Y. Zhang and W. Yang, Phys. Rev. Lett. **80** (4), 890 (1998).

[46] S. Grimme, J. Antony, S. Ehrlich, and H. Krieg, J. Chem. Phys. **132** (15), 154104 (2010).

[47] S. Grimme, S. Ehrlich, and L. Goerigk, J. Comput. Chem. **32** (7), 1456–1465 (2011). doi:10.1002/jcc.21759.

[48] K. Mathew, R. Sundararaman, K. Letchworth-Weaver, T.A. Arias, and R.G. Hennig, J. Chem. Phys. **140** (8), (2014). doi:10.1063/1.4865107.

[49] G. Henkelman, B.P. Uberuaga, and H. Jónsson, J. Chem. Phys. **113** (22), 9901–9904 (2000). doi:10.1063/1.1329672.

[50] P. Pulay, Chem. Phys. Lett. **73** (2), 393–398 (1980). doi:10.1016/0009-2614(80)80396-4.

[51] L. Verlet, Phys. Rev. **159** (1), 98–103 (1967). doi:10.1103/PhysRev.159.98.

[52] W.K. Den Otter and W.J. Briels, Mol. Phys. **98** (12), 773–781 (2000). doi:10.1080/00268970009483348.

[53] J.-P. Ryckaert, G. Ciccotti, and H.J.C. Berendsen, J. Comput. Phys. **23** (3), 327–341 (1977). doi:10.1016/0021-9991(77)90098-5.

[54] F. Libisch, C. Huang, and E.A. Carter, Acc. Chem. Res. **47** (9), 2768–2775 (2014).

[55] K. Yu, C. M. Krauter, J. M. Dieterich, and E. A. Carter, in *Fragmentation: Toward Accurate Calculations on Complex Molecular Systems*, edited by Mark Gordon (Wiley Online Books, 2017, 81–117). doi:10.1002/9781119129271.ch2.

[56] C. Huang, M. Pavone, and E.A. Carter, J. Chem.: Phys. **134** (15), 154110 (2011). doi:10.1063/1.3577516.

[57] K. Yu, F. Libisch, and E.A. Carter, J. Chem. Phys. **143** (10), 102806 (2015). doi:10.1063/1.4922260.

[58] EmbeddingIntegralGenerator. https://github.com/EACcodes/EmbeddingIntegralGenerator.

[59] VASPEmbedding; github. https://github.com/EACcodes/VASPEmbedding.

[60] W. Yang and Q. Wu, Phys. Rev. Lett. **89** (14), 143002 (2002). doi:10.1103/PhysRevLett.89.143002.

[61] M. Head-Gordon, J.A. Pople, and M.J. Frisch, Chem. Phys. Lett. **153** (6), 503–506 (1988). doi:10.1016/0009-2614(88)85250-3.

[62] F. Weigend and R. Ahlrichs, Phys. Chem. Chem. Phys. **7** (18), 3297–3305 (2005). doi:10.1039/B508541A.

[63] H.-J. Werner, P.J. Knowles, F.R. Manby, J.A. Black, K. Doll, A. Heßelmann, D. Kats, A. Köhn, T. Korona, D.A. Kreplin, et al., J. Chem. Phys. **152** (14), 144107 (2020). doi:10.1063/5.0005081.

[64] J.-N. Boyn and E.A. Carter, J. Am. Chem. Soc. **145** (37), 20462–20472 (2023). doi:10.1021/jacs.3c06182.

[65] K.R. Bryenton, A.A. Adeleke, S.G. Dale, and E.R. Johnson, WIREs Com. Mol. Sci. **13** (2), e1631 (2023). doi:10.1002/wcms.1631.

[66] J.-N. Boyn and E.A. Carter, J. Phys. Chem. B. **127** (50), 10824–10832 (2023). doi:10.1021/acs.jpcb.3c05369.